Title

Age-Related Brain Atrophy and the Positive Effects of Behavioral Enrichment in Middle-Aged Beagles

Authors

Noche, Jessica A

Radhakrishnan, Hamsanandini

Ubele, Margo F

et al.

Neurobiology of Disease

Age-Related Brain Atrophy and the Positive Effects of Behavioral Enrichment in Middle-Aged Beagles

Jessica A. Noche,[1] Hamsanandini Radhakrishnan,[1,2] Margo F. Ubele,[3] Kathy Boaz,[3] Jennifer L. Mefford,[3] Erin D. Jones,[3] Hollie Y. van Rooyen,[3] Jessica A. Perpich,[3] Katie McCarty,[3] Beverly Meacham,[3] Jeffrey Smiley,[3] Stasia A. Bembenek Bailey,[3] László G. Puskás,[4] David K. Powell,[3] Lorena Sordo,[1] Michael J. Phelan,[1] Christopher M. Norris,[3] Elizabeth Head,[1] and Craig E.L. Stark[1]

[1]University of California, Irvine, California 92697, [2]University of Pennsylvania, Philadelphia, Pennsylvania 19104, [3]University of Kentucky, Lexington, Kentucky 40506, and [4]Aperus Pharma, Szeged H-6726, Hungary

Aging dogs serve as a valuable preclinical model for Alzheimer's disease (AD) due to their natural age-related development of β-amyloid (Aβ) plaques, human-like metabolism, and large brains that are ideal for studying structural brain aging trajectories from serial neuroimaging. Here we examined the effects of chronic treatment with the calcineurin inhibitor (CNI) tacrolimus or the nuclear factor of activated T cells (NFAT)-inhibiting compound Q134R on age-related canine brain atrophy from a longitudinal study in middle-aged beagles (36 females, 7 males) undergoing behavioral enrichment. Annual MRI was analyzed using modern, automated techniques for region-of-interest-based and voxel-based volumetric assessments. We found that the frontal lobe showed accelerated atrophy with age, while the caudate nucleus remained relatively stable. Remarkably, the hippocampus increased in volume in all dogs. None of these changes were influenced by tacrolimus or Q134R treatment. Our results suggest that behavioral enrichment can prevent atrophy and increase the volume of the hippocampus but does not prevent aging-associated prefrontal cortex atrophy.

Key words: Alzheimer's disease; amyloid; beagle; calcineurin; neurodegeneration; prevention; Q134R; tacrolimus

---

Significance Statement

Aging canines naturally show significant neuropathological similarities to human aging and AD, making them valuable translational models for testing disease-modifying treatments. We applied modern, state-of-the-art longitudinal volumetric analysis approaches to evaluate treatment effects from structural MRI in a large cohort of middle-aged beagles treated with the FDA-approved calcineurin inhibitor, tacrolimus, or the experimental NFAT inhibitor, Q134R, while undergoing extensive behavioral enrichment. We show increased hippocampal volumes across all dogs, even control placebo dogs, providing compelling evidence for a strong enrichment-related benefit on hippocampal structural integrity. Our findings are the first of its kind to demonstrate benefits of behavioral intervention on longitudinal structural brain changes in a higher mammalian model of aging and AD.

Introduction

Canines share aging-related neuropathological features with humans, making for a valuable translational model for

Alzheimer's disease (AD). Aging canines intrinsically develop diffuse β-amyloid (Aβ) pathology that is associated with cognitive decline akin to human mild cognitive impairment (MCI; Cotman and Head, 2008). Furthermore, cognitive functions tested in beagles that are relevant in AD, including spatial memory and executive function, are vulnerable to aging and Aβ burden (Head et al., 1998; Chan et al., 2002; Tapp et al., 2003; Rofina et al., 2006; Studzinski et al., 2006). Their drug tolerance and metabolism align with humans as well (Martinez et al., 2021). Furthermore, the larger, gyrencephalic brain of beagles compared with lower mammalian AD models proves advantageous for in vivo structural assessments with magnetic resonance imaging (MRI) and for larger sampling volumes for postmortem histological evaluations. These features, coupled with their shorter

lifespans relative to humans, make them ideal for studying longitudinal effects of behavioral and pharmacological interventions (Su et al., 2005; Head et al., 2008; Araujo et al., 2022).

Clinical trials in AD patients often target the classic pathological hallmarks, the aggregation of Aβ plaques or tau neurofibrillary tangles (Perl, 2010; Congdon and Sigurdsson, 2018), but have failed to result in effective therapies. Investigations of preventative therapeutics targeting alternative dysfunctional mechanisms are thus warranted (Crous-Bou et al., 2017). A promising target is the hyperactive signaling of the Ca^{2+}/calmodulin-dependent protein phosphatase calcineurin and its substrate transcription factor, the nuclear factor of activated T cells (NFATs). Aβ plaque aggregation is linked to aberrant calcineurin/NFAT hyperactivity within neurons and astrocytes, leading to neuroinflammation, Ca^{2+} dysregulation, synaptic dysfunction, and excitotoxicity (Norris et al., 2005; Kuchibhotla et al., 2008; Reese and Taglialatela, 2010). This hyperactivity is associated with cognitive dysfunction in transgenic AD models (Sompol et al., 2017) and in early AD patients (Abdul et al., 2009, 2011). Calcineurin inhibition ameliorates these effects in transgenic mouse models of AD (Taglialatela et al., 2009; Stallings et al., 2023) and was previously linked to a profound reduction in dementia incidence among solid organ transplant patients maintained on calcineurin inhibitors (Taglialatela et al., 2015). Our group recently showed that a low dose of the FDA-approved calcineurin inhibitor (CNI) tacrolimus protected against age-related microstructural gray matter changes within the hippocampus, parahippocampal gyrus, and prefrontal cortex of middle-aged beagles compared to placebo-treated dogs after 1 year (Radhakrishnan et al., 2021). This offers promising evidence for the potential of tacrolimus repurposed as a preventative treatment of AD.

Postmortem evaluations in beagles describe typical age-related characteristics across the canine lifespan in great detail (Vite and Head, 2014), but in vivo characterizations are limited. Of the available cross-sectional MRI studies in beagles, findings largely align with postmortem evidence of ventricular widening (González-Soriano et al., 2001; Kimotsuki et al., 2005), early vulnerability of the frontal lobe, (Tapp et al., 2004), and later vulnerability of the hippocampus to neuron loss (Tapp et al., 2004). However, there are individual differences among aging canines, even within the same breed, that parallel the structural heterogeneity of the aging human brain and add ambiguity to cross-sectional examinations (Cotman and Head, 2008). Furthermore, age and cohort effects pose additional challenges to interpretations of cross-sectional findings (O'Brien, 2017).

Longitudinal studies are fundamentally immune to such effects and allow for direct assessments of individual trends over time. While prior MRI studies in aging canines qualitatively assessed neuroanatomy (Gross et al., 2010) or employed visually guided methods for large-scale brain aging characteristics (Su et al., 2005), visual inspection alone falls short in detecting subtle alterations during aging or assessing long-term interventional effects often measured at the submillimeter level in histological evaluations.

Innovative software for analyzing human neuroimaging data have been successfully applied to just a handful of canine studies but have regularly required some user intervention for standard preprocessing procedures including brain extraction (Milne et al., 2016), or for delineating brain regions (Tapp et al., 2004), which can be time-consuming and prone to user error when manually performed. Hence, an analytical framework for applying automated and standardized methods for reliable longitudinal analysis for canine imaging data is necessary for enhancing reproducibility and translating neuroimaging biomarker endpoints to clinical trial outcomes.

To this end, we leveraged advanced, open-source image analysis tools to evaluate structural alterations in a prevention study in healthy middle-aged beagles undergoing chronic CN/NFAT inhibitor treatment and behavioral enrichment. Regional volume changes were assessed using atlas-based volumetry as well as deformation-based morphometry (DBM) from high-resolution T1-weighted imaging collected annually for 3 years. We hypothesized that aging would be associated with brain region-specific losses in volume that may be protected by a combination treatment approach with behavioral enrichment and CN or NFAT inhibitor treatment.

Materials and Methods

Experimental design

Animals

The study began with 45 purpose-bred intact adult beagles assessed for general health status and cognition, as previously described (Head et al., 1998; Milgram et al., 1999; Tapp et al., 2003; Studzinski et al., 2006; Christie et al., 2008; Perl, 2010). The final sample included 43 dogs (36 females, 7 males) ranging from 5 to 8.7 years old. The dogs were then divided into three groups. One group was treated with a placebo ($n = 14$) while two groups were treated with a chronic low dose of the FDA-approved CNI tacrolimus ($n = 15$) or the NFAT-inhibiting small chemical compound Q134R (Hackler et al., 2019; Sompol et al., 2021; $n = 14$) as part of a longitudinal preclinical study investigating their potential for preventing AD-related pathology when treated in middle age (Fig. 1). Tacrolimus was given at 0.075 mg/kg (twice daily, p.o.). Dosage for Q134R was increased after the first year of treatment from 4 mg (twice daily, p.o.) to 8 mg (twice daily, p.o.) for years 2 and 3. Prior to reaching the third MRI scanning session (T3), two dogs spontaneously developed health conditions unrelated to treatment that were unable to be sufficiently managed with medical intervention and were excluded from subsequent procedures and analyses (Table 1).

Blood samples were taken every 6 months to monitor overall health and potential adverse effects via assessments of blood urea nitrogen, creatine, and phosphorous levels since tacrolimus can cause nephrotoxicity in solid organ transplant patients at higher doses (Randhawa et al., 1997). All institutional and national guidelines for the care and use of laboratory animals were followed.

Behavioral enrichment

The behavioral enrichment paradigm consisted of daily exercise, socialization, cognitive testing, rotating toys, and social compatible group indoor/outdoor free play. Free play was provided for 30 min and in male-only or female-only groups. Sex-matched dogs were pair-housed in the mornings and split into their individual kennels in the afternoon prior to feeding. Six sets of two play objects were rotated through each kennel at weekly intervals. Furthermore, dogs were trained and tested on a battery of neurocognitive tests designed to capture age-related decline across several cognitive domains. Briefly, the tasks included spatial learning and memory tasks, landmark discrimination, oddity discrimination, size discrimination, black/white discrimination, as well as reversal learning. Detailed descriptions of these tasks are described by Davis et al. (2017). The dogs were tested at baseline prior to receiving treatment and continuously trained and tested on these tasks 5 d/week (20–40 min depending on the task) throughout the entirety of the study.

Neuroimaging

Imaging data acquisition. Imaging data were collected at the Magnetic Resonance Imaging and Spectroscopy Center (MRISC) at the University of Kentucky in Lexington, Kentucky. Animals were fasted overnight and placed under general anesthesia using propofol (4–8 mg/kg, i.v., by slow injection to effect). Following induction and orotracheal intubation, anesthesia was maintained with 1–4% isoflurane delivered in 100% O_2
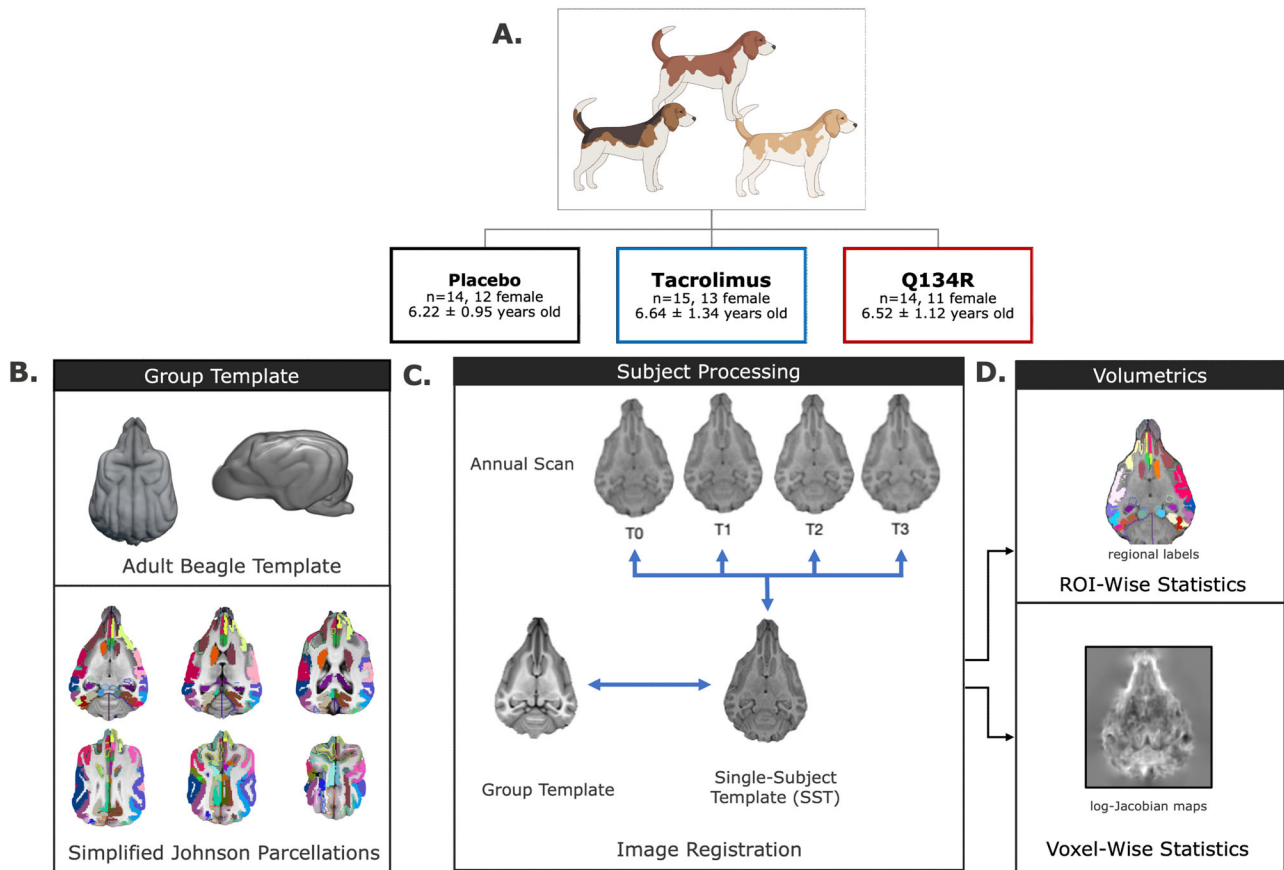
Figure 1. Treatment groups and the longitudinal image processing pipeline for measuring ROI-based and voxel-wise volumes. *A*, Middle-aged beagles were divided into three treatment groups: placebo ($n = 14$), tacrolimus ($n = 15$), and Q134R ($n = 14$) that all underwent continuous behavioral enrichment and annual neuroimaging. *B*, A high-resolution group template that was previously developed from a subset of beagles at baseline was used as common template space. A simplified version of the cortical/subcortical atlas developed by Johnson et al. (2020) was then coregistered to the group template for ROI-based statistics (unfilled regions were excluded from analysis). *C*, For individual subject processing, the pipeline first constructed an unbiased single-subject template (SST) from all available time point images which served as an unbiased intermediate space for registration between the group template and each individual time point. Each time point image underwent preprocessing with reference to the SST where bidirectional spatial transformations were generated and applied (blue arrows). *D*, The atlas was mapped onto each time point image to calculate ROI volumes. The log-Jacobian maps were derived from the nonlinear spatial transformations for each time point image and were used to perform deformation-based morphometry (DBM), a voxel-wise method for brain-wide volume analysis. Created with BioRender.com.

Table 1. Dog characteristics

Group	N	Age at start	Sex
Placebo	14	6.23 ± 0.95	12F, 2M
Tacrolimus	15	6.64 ± 1.34	13F, 2M
Q134R	14	6.53 ± 1.12	11F, 3M

Ages are presented as mean ± standard deviation (SD).

during MRI scanning. As part of the standard protocol, dogs were also premedicated with 0.4 mg/kg of meloxicam as a prophylaxis for CSF collection-induced soft-tissue injury and headache/nausea. All CSF collections were completed post-MRI. A 3T MRI scanner (Siemens Prisma Fit) with a 15-channel transmit–receive knee coil was used to scan the canine brain across four time points: at baseline before treatment with placebo, tacrolimus or Q134R (T0), and annually for 3 years (T1–T3). For structural imaging, a high-resolution T1-weighted image was collected using a magnetization-prepared rapid gradient-echo (MPRAGE) sequence [repetition time (TR), 2,530 ms; echo time (TE), 2.49 ms; flip angle, 7°; matrix size, $0.4 \times 0.4 \times 0.7$ mm; averages, 1; average acquisition time, 10 min, 30 s; voxel size, 0.352×0.352 mm; slice thickness, 0.7 mm].

Image processing. The T1-weighted images were first visually inspected for quality control. No obvious adverse effects of treatment on brain structure were identified for any dogs. Minor ghosting artifacts that did not overlap with the brain were edited out from the 3D images of two dogs to overcome faulty registration during image preprocessing. Next, all images were processed using the Advanced Normalization Tools (ANTs) software (version 2.3.1). ANTs has an extensive track record of robust performance in lifespan analyses of brain morphology (Tustison et al., 2014) and has been recently implemented in canine neuroimaging studies for the development of in vivo and ex vivo group templates and digital atlases (Datta et al., 2012; Czeibert et al., 2019; Johnson et al., 2020). The high-resolution group template developed for an earlier report on the tacrolimus-treated and placebo-treated dogs was used in the present study (Radhakrishnan et al., 2021). For atlas-based ROI analyses, we used a recently developed high-resolution stereotaxic canine brain atlas with detailed parcellations (Johnson et al., 2020) and created a simplified version by grouping cortical parcellations by their respective gyri. This simplified atlas, hereby referred to as the "Johnson atlas," was registered to the group template space using the affine + SyN algorithm for diffeomorphic image registration. Finally, CSF posteriors were obtained from processing the group template through the ANTs cortical thickness pipeline and were added to the CSF segmentation map by Johnson et al. (2020) which was then binarized and smoothed to create a more detailed CSF prior probability map that can better resolve CSF compartments within narrow sulci.

Individual image processing was then performed using a longitudinal image analysis pipeline newly available within ANTs that has

Table 2. ROI volume slope statistics for the entire group of dogs on the 24 bilateral ROIs from 7 lobar locations (Johnson et al., 2020)

Lobe	Region	T0 volume ± SD (mm³)	Median slope (IQR)	Median slope rank (IQR)	t statistic (slope 0)	p value
Frontal	Orbital gyrus	652.48 ± 70.75	−0.165 (0.15)	5 (6)	−7.787	<0.001***
	Pregenual gyrus	225.86 ± 21.69	−0.153 (0.20)	6 (8.5)	−7.875	<0.001***
	Gyrus proreus	235.91 ± 49.63	−0.211 (0.27)	5 (10.5)	−5.766	<0.001***
Sensory-motor	Anterior compositus gyrus	727.67 ± 76.88	−0.121 (0.21)	10 (11)	−3.498	0.0088**
	Precruciate	547.19 ± 68.59	−0.138 (0.19)	8 (9.5)	6.375	<0.001***
Cingulate	Genualis	146.08 ± 16.65	−0.001 (0.19)	17 (8.5	−0.291	0.9713
	Anterior cingulate gyrus	108.95 ± 9.91	−0.115 (0.16)	10 (8)	−5.890	<0.001***
	Medial cingulate gyrus	118.43 ± 11.73	−0.071 (0.15)	13 (10)	−4.066	0.0022**
	Posterior cingulate gyrus	375.43 ± 36.94	−0.121 (0.20)	10 (9)	−5.035	<0.001***
Occipital	Medial occipital gyrus	1163.82 ± 108.14	−0.078 (0.10)	14 (6)	−5.444	<0.001***
	Recurrens	192.04 ± 30.91	−0.163 (0.20)	11 (13)	−5.300	<0.001***
	Pararecurrens	211.77 ± 24.82	−0.118 (0.20)	8 (13.5)	−6.048	<0.001***
	Suprasylvian gyrus	1285.17 ± 148.69	−0.044 (0.11)	17 (6.5)	0.019	0.9849
	Lateral fissure	233.51 ± 29.37	−0.051 (0.10)	15 (9.5)	−3.690	0.0054**
Parietal	(PR) Coronal gyrus	230.87 ± 31.41	−0.018 (0.09)	16 (6.5)	−0.567	0.967
	Presplenial gyrus	170.29 ± 17.94	−0.100 (0.16)	12 (9.5)	−4.967	<0.001***
	Entolateral gyrus	459.11 ± 73.22	0.015 (0.18)	18 (10)	0.769	0.948
	(PR) Marginal gyrus	230.55 ± 22.68	−0.101 (0.21)	11 (10)	−2.767	0.0494*
Temporal	Posterior compositus gyrus	594.14 ± 69.97	−0.181 (0.15)	6 (6.5)	−8.246	<0.001***
	Ectosylvian gyrus	1677.71 ± 162.77	−0.072 (0.10)	14 (4)	−3.212	<0.001***
	Sylvian gyrus	1027.48 ± 108.43	−0.143 (0.09)	8 (5.5)	−8.559	<0.001***
Subcortical	Amygdala	124.57 ± 11.86	−0.008 (0.14)	17 (10)	−0.397	0.9713
	Caudate nucleus	483.14 ± 44.38	0.056 (0.13)	22 (4.5)	4.093	0.0022**
	Hippocampus	520.39 ± 50.12	0.158 (0.11)	24 (2)	7.447	<0.001***

Volume-over-time slopes were ranked per dog for nonparametric rank-sum analyses (Fig. 2). One-sample t tests were additionally used to test for nonzero slopes; the resulting p values were adjusted by the Holm–Sidak method for multiplicity. PR, part of the ROI spanning the parietal lobe; IQR, interquartile range. *p < 0.05, **p < 0.01, ***p < 0.001.

demonstrated superior performance in humans for detecting disease-related structural alterations from serial neuroimaging (Tustison et al., 2019) and interventional effects in clinical trials (Song et al., 2022). Here, minor customizations were made to the pipeline to account for canine brain size and voxel dimensions. An important feature of this pipeline is the creation of an unbiased single-subject template (SST) used as an intermediate reference space between the group template and time point images for reducing registration errors and optimizing sensitivity to longitudinal volume changes (Fig. 1). In the pipeline, each dog's SST was first generated from its set of T1-weighted images that underwent preprocessing including N4 bias-field correction (Tustison et al., 2010), brain extraction, and probabilistic tissue segmentation via Atropos (Avants et al., 2011) with reference to the group template, resulting in prior probability maps in the space of the SST as well as nonlinear SST to group template warps. Each time point image was then rigidly aligned to the SST and denoised prior to undergoing the same preprocessing steps as the SST while treating the SST as the reference template, resulting in tissue segmentation maps and warps to the SST for each time point image.

ROI-based volumetry. To obtain regional volume measures at each time point, the Johnson atlas was registered to the processed time point images by applying the warps generated from combining the template to SST and SST to time point warps. The volume of each region was calculated in each dog's native time point space as the sum of all voxels within each atlas parcellation with CSF voxels subtracted and converted to cubic millimeters. The left and right ROI volumes were adjusted by the log-Jacobian determinant of the linear SST to group template transformation of each animal, a scalar value associated with approximate intracranial volume (ICV; Buckner et al., 2004) and z-transformed with respect to each ROI's mean baseline volume. We did not observe any significant differences between bilateral ROIs at baseline so mean bilateral volumes were calculated for subsequent analysis.

Several cortical ROIs and the cerebellum were excluded from further analysis due to erroneous tissue segmentations at brain versus nonbrain boundaries for several dogs at various time points. Brainstem and claustrum ROIs defined within the original Johnson atlas were not included in the analysis. A final total of 24 bilateral ROIs were examined that

included cortical structures from frontal, sensory-motor, cingulate, occipital, parietal lobar areas, as well as three subcortical structures: amygdala, caudate nucleus, and hippocampus (Table 2).

Deformation-based morphometry. As a complimentary volumetric analysis, we performed DBM for a more granular, voxel-based assessment of volume changes. Briefly, maps of the nonlinear warps generated from voxel-wise registration of each image to a reference image in the same coordinate space (e.g., the time point image moving to the SST) can be converted to a log-Jacobian determinant map which represents the amount of expanding or contracting of each voxel during the registration. When registering to a common template space, the log-Jacobians can be considered a voxel-based summary measure of volume that can be compared across individuals (Ashburner et al., 1998). Here, we combined the warps generated from the time point to the SST registration and SST to the group template registration during preprocessing. Creating "DBM maps" by this method, these maps are set in the group template space that captures each dog's longitudinal changes with respect to its SST as well as cross-sectional differences with respect to the group template. Each DBM map was resampled to a 0.5 mm isotropic resolution and was slightly eroded by two voxels to exclude problematic edge voxels that were found to include CSF, pia, or dura in several dogs' native space (Fig. 1).

Statistical analysis

ROI volumetry. First, for an initial evaluation of general atrophy rates regardless of treatment group, we calculated simple ROI volume slopes over time for each dog from bivariate ordinary least squares regressions. We then used a nonparametric rank analysis for evaluating differences between regional atrophy rates using the Friedman test. We performed post-hoc pairwise comparisons of rank-sum differences as well as one-sample t tests against zero on each set of ROI slopes. All pairwise comparisons were adjusted for multiplicity using the Holm-Sidak post-hoc test from the SciPy library in Python.

Next, we conducted separate multivariate linear mixed effects (LME) analyses per ROI. LME models can flexibly account for incomplete data, dependency within repeated within-subjects measurements, and hierarchically structured data, which can improve the reproducibility of

longitudinal studies (Yu, Guindani, et al., 2022). To predict ROI volume, we assigned treatment group, baseline age, years elapsed since the initial baseline scan ("time"), and a time-by-treatment interaction term as fixed effects, and a random intercept was assigned at the level of individual dogs (i.e., random effect of subject). The p values for the LME parameter estimates from each ROI analysis were adjusted for multiple comparisons using the Holm–Sidak method for a family-wise error rate of 5%.

Lastly, we used an all-ROI-inclusive LME model by adding "region" as a predictor variable to evaluate differential patterns of volume changes in a single model using the hippocampus as the reference level. The region with the least decline observed from the two prior analyses was used as the reference ROI in the model. Since the per-region LME models did not show reliable evidence for treatment by time interactions (Fig. 4), the treatment predictor was excluded from this LME analysis to evaluate sample-wide trends in volume changes regardless of treatment group. Thus, the fixed effects for this model included region, time, z-transformed baseline age, a time by region interaction term, and a random intercept was again assigned per dog. Here, the estimates for baseline age and time attributed to the reference region, and the estimates for each time by region interaction are thus conditional on the estimated effect of time. Diagnostic model fit evaluations using the Akaike Information Criterion (AIC) and the Bayesian Information Criterion (BIC) indicated that a model excluding treatment was indeed preferred over a model that included interactions with treatment.

DBM analysis. We conducted a brain-wide LME analysis of voxel-wise volume change on the DBM maps using the 3dLMEr package in the Analysis of Functional NeuroImages (AFNI) software suite (Chen et al., 2013). Here, treatment group, baseline age, time, and a time-by-treatment interaction term were assigned as fixed effects, and a random effect was

assigned per dog for predicting the log-Jacobian determinant (i.e., volume) per voxel. Baseline age values were centered on the mean baseline age of 6.7 years (age − mean age) and time was centered on baseline year (time, 0). Minimum cluster size thresholds for the z-statistical maps of each main effect, interaction, and treatment contrasts over time (tacrolimus over time vs placebo over time, Q134R over time vs placebo over time), correcting for multiple comparisons, were empirically determined from 100 Monte Carlo simulations in 3dLMEr. Baseline age and treatment were permuted across subjects, and time was permuted within subjects. Each critical cluster size was determined from the 5% probability of the largest resulting false-positive clusters generated using AFNI's 3dClusterize with a voxel-wise threshold of $p = 0.0001$.

Code availability
Code for data processing and analysis is available at https://github.com/StarkLabUCI/canine-long-sMRI.

Results

Regional selectivity of volume losses, hippocampal volume increases
First, rank analyses of the dog-specific slopes of volume over time revealed consistent patterns of cortical volume loss among 17 cortical ROIs (Fig. 2A,B; Table 2). All frontal lobe ROIs, including the pregenual, proreus, and orbital gyri, were ranked highest for exhibiting the most rapid rates of volume loss [orbital gyrus: median slope (z) = −0.17, median rank = 5 out of 24; gyrus proreus: median slope = −0.21, median rank = 5; pregenual gyrus: median slope = −0.15, median rank = 6; Fig. 3] and declined significantly faster
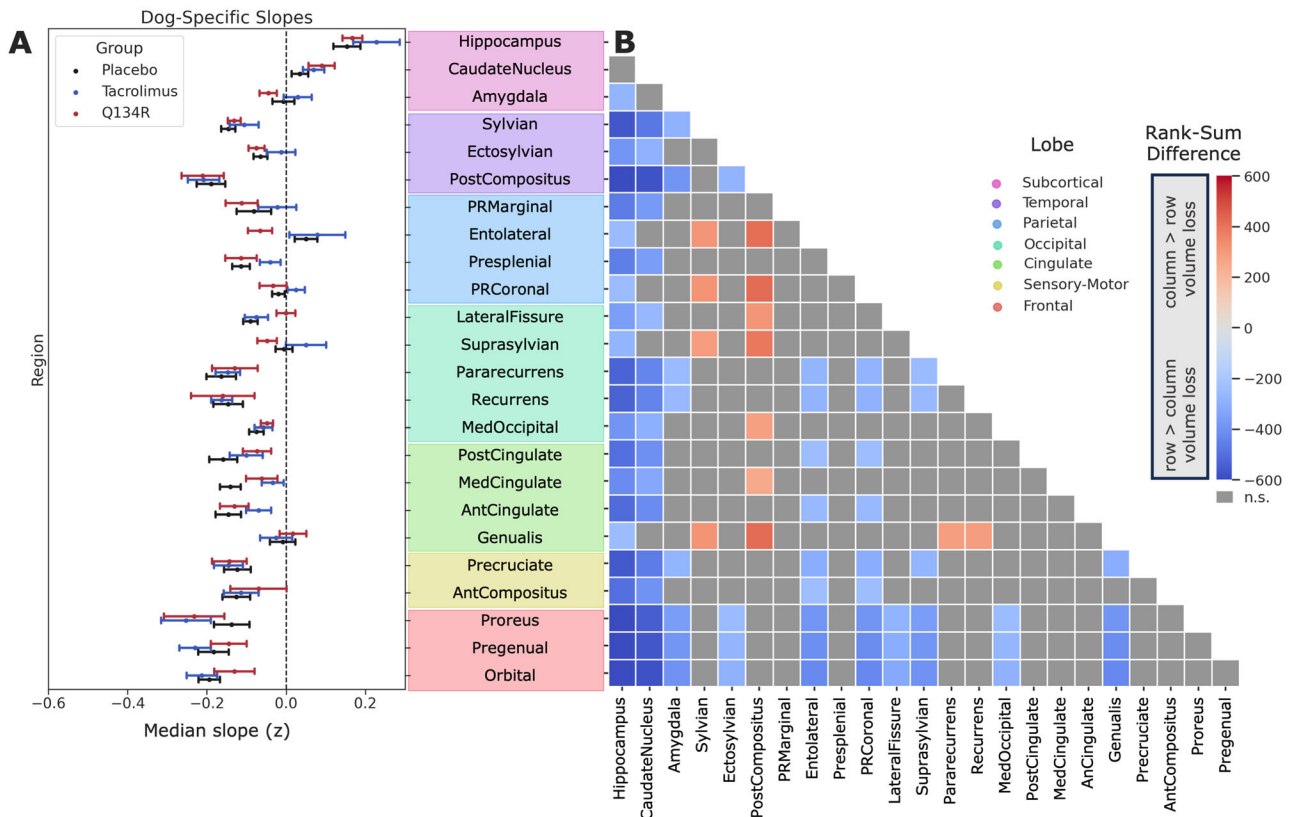
Figure 2. Differential pattern of ROI volume decline from dog-specific simple volume slopes. ***A***, The mean (circle) and standard error (bars) of the dog-specific volume slopes over time (z-scored) for each treatment group (black, placebo; blue, tacrolimus; red, Q134R). ***B***, All groups showed similar patterns of volume decline, so treatment groups were combined. We performed a nonparametric analysis of variance to evaluate pair-wise differences in volume changes by their slope-rank sums (Table 2). Cooler colors represent more rapid volume loss for the row ROI versus the column ROI, and warmer colors represent greater rates of volume loss for the column ROI versus the row ROI. Pair-wise differences that did not reach statistical significance (>adjusted p-threshold 0.05) are in gray.
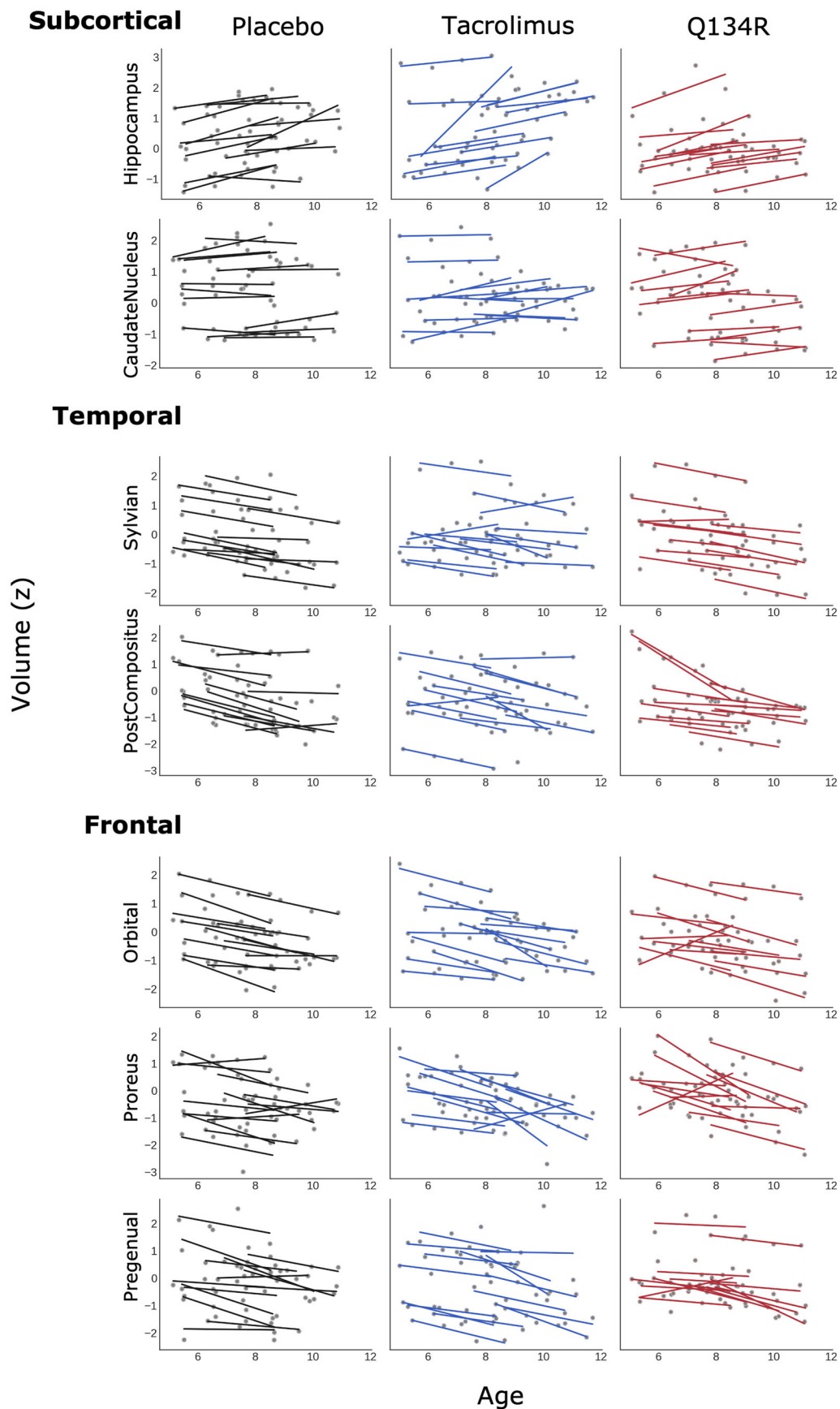
Figure 3. Simple slopes per dog over time for ROIs with greatest changes in subcortical, temporal, and frontal lobes. Cortical ROIs in frontal and temporal lobes ranked highest for the most rapid volume decline. Conversely, the hippocampus showed volume increases across nearly all of the dogs, and the caudate nucleus volumes were preserved over time with some dogs showing slight volume increases.
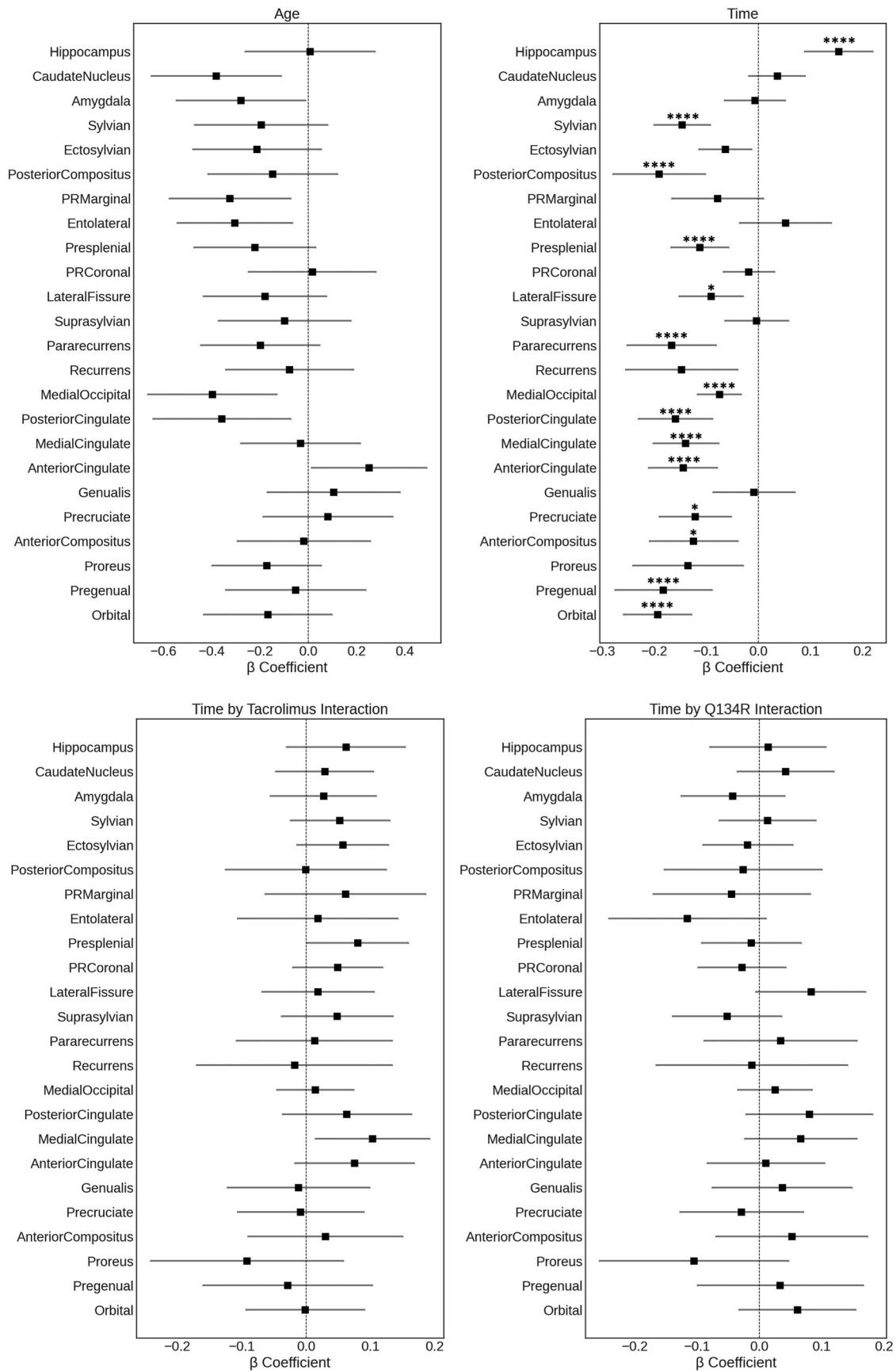
Figure 4. Beta coefficient estimates for baseline age, time, time by tacrolimus interactions, and time by Q134R interactions. Only main effects of time showed reliable trends of volumetric decreases with the exception of the hippocampus which showed increases over time from the separate linear mixed effects models per region. *p* values were adjusted for multiple comparisons using the Holm–Sidak method. *$p < 0.05$, **$p < 0.01$, ***$p < 0.001$, ****$p < 0.0001$. Beta coefficients without asterisks were $p > 0.05$.
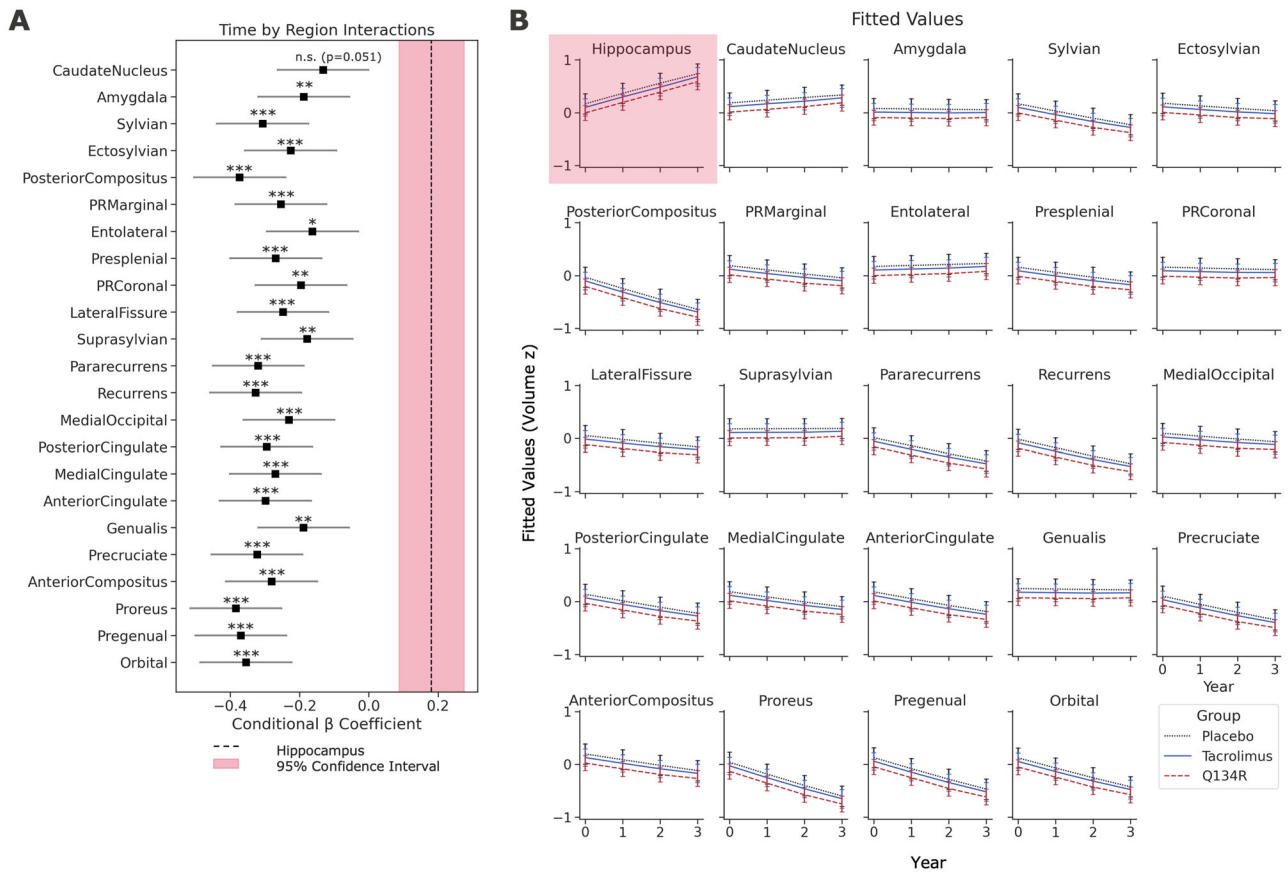
Figure 5. Contrasting the volume trajectories directly against the hippocampus in an all-ROI-inclusive LME model. **A**, The conditional beta coefficients of the ROIs for the time by region interactions (black squares) and the 95% confidence interval (lines) are selectively shown out of the full set of parameter estimates (Table 3). Along with demonstrating differential patterns of volume decline, this modeling approach clearly demonstrates that the volume trajectories of every ROI strongly differ from the estimated annualized increase observed in the hippocampus (dotted line, 95% confidence interval in crimson). *$p \leq 0.05$, **$p \leq 0.01$, ***$p \leq 0.001$. **B**, Fitted volumes of each ROI at each time point with the reference region in the model highlighted in crimson. Groups were plotted separately for visualization only; the model did not include group as a predictor since no significant group effects were found in the per-region LME analyses (Fig. 4).

than 10 other regions (Fig. 2B). Furthermore, the posterior compositus and sylvian gyri within the temporal lobe ranked next highest for rapid volume loss (posterior compositus gyrus: median slope = −0.18, median rank = 6; sylvian gyrus: median slope = −0.14, median rank = 8). There was no apparent evidence of volume loss from the simple volume slopes of the genualis, suprasylvian, parietal coronal, and entolateral gyri or from the amygdala (Table 2). Most notably and contrary to typical brain aging in canines (Tapp et al., 2004; Kimotsuki et al., 2005; Su et al., 2005), the hippocampus showed strong evidence of unique volumetric increases over time (median slope = 0.16, median rank = 24) and the caudate nucleus also showed evidence for a mild volumetric increase (median slope = 0.06, median rank = 22; Figs. 2B,C, 3; Table 2). The remaining regions in the cingulate, sensory-motor, occipital, and parietal lobes also showed volume loss but to a lesser extent (Fig. 2C, Table 2).

Next, we employed separate multivariate LME models per ROI to test for longitudinal effects of treatment and baseline age on volume losses as a function of time. We did not observe any significant time-by-treatment interactions for tacrolimus or Q134R for any ROIs after adjusting for multiple comparisons. The regions that showed a significant main effect of time on volume loss were largely consistent with the regions found to decline in the above simple slope analyses. However, we found that the LME models for the ectosylvian, parietal marginal, recurrens, and proreus gyri, and the caudate nucleus did not show sufficient

evidence of any volume changes over time (Fig. 4). A strong increase in hippocampal volume over time across all groups was also evident by LME analysis ($\beta = 0.154$; SE = 0.034; adjusted $p < 0.001$; CI[0.088, 0.220]).

The noteworthy increases in hippocampal volume across all groups motivated the use of the larger, all-ROI-inclusive LME analysis to directly contrast its rate of decline to that of each ROI in a single model. Here, the parameter estimates for each ROI are conditional upon the main effects of time and age, with the volume of the hippocampus as the reference region (Fig. 5A). Treatment group was excluded from this model due to the lack of evidence for treatment effects in every per-region LME analysis. We found volume increases in hippocampal volume over time as we observed in our prior analyses ($\beta = 0.181$; SE = 0.048; $p < 0.001$; CI[0.087, 0.275]), which equates to a 1.74% average annual increase in volume. Critically, every time-by-region interaction apart from the caudate nucleus showed distinct rates of volume decline relative to the hippocampus, underscoring the unique trajectory of hippocampal volume changes over the 3 years. Furthermore, the differential pattern of volume decline across the other ROIs were highly consistent with the simple slope analysis, specifically the accelerated volume decline of frontal pregenual, proreus, and orbital gyri and temporal posterior compositus gyrus (Fig. 5A,B). The full set of parameter estimates for this model can be found in Table 3.

Table 3. Parameter estimates from the all-ROI-inclusive LME model for predicting volumes by normalized baseline age (BAge) years in study (time), and region, where the hippocampus was assigned as the reference level for the region predictor

Predictor	Level	Coef.	Std. err.	z	p>|z|	95% CI (lower-upper)
Intercept	Reference=Hippocampus	0.088	0.131	0.668	0.504	[−0.17, 0.345]
Region	Amygdala	−0.089	0.133	−0.67	0.503	[−0.35, 0.172]
	Anterior cingulate	0.016	0.133	0.122	0.903	[−0.245, 0.277]
	Anterior compositus	0.03	0.133	0.226	0.821	[−0.231, 0.291]
	Caudate nucleus	0.015	0.133	0.112	0.911	[−0.246, 0.276]
	Ectosylvian	0.01	0.133	0.075	0.94	[−0.251, 0.271]
	Entolateral	0.003	0.133	0.02	0.984	[−0.258, 0.264]
	Genualis	0.078	0.133	0.583	0.56	[−0.183, 0.339]
	Lateral fissure	−0.114	0.133	−0.853	0.394	[−0.375, 0.147]
	Medial cingulate	0.019	0.133	0.139	0.889	[−0.242, 0.279]
	Medial occipital	−0.071	0.133	−0.536	0.592	[−0.332, 0.19]
	Orbital	−0.045	0.133	−0.338	0.735	[−0.306, 0.216]
	PR coronal	−0.01	0.133	−0.075	0.94	[−0.271, 0.251]
	PR marginal	0.018	0.133	0.139	0.89	[−0.242, 0.279]
	Pararecurrens	−0.155	0.133	−1.164	0.245	[−0.416, 0.106]
	Posterior cingulate	−0.029	0.133	−0.216	0.829	[−0.29, 0.232]
	Posterior compositus	−0.203	0.133	−1.524	0.127	[−0.464, 0.058]
	Precruciate	−0.063	0.133	−0.476	0.634	[−0.324, 0.198]
	Pregenual	−0.04	0.133	−0.3	0.764	[−0.301, 0.221]
	Presplenial	−0.012	0.133	−0.087	0.93	[−0.273, 0.249]
	Proreus	−0.128	0.133	−0.959	0.338	[−0.389, 0.133]
	Recurrens	−0.183	0.133	−1.376	0.169	[−0.444, 0.078]
	Suprasylvian	0.013	0.133	0.094	0.925	[−0.248, 0.273]
	Sylvian	0	0.133	−0.004	0.997	[−0.261, 0.26]
BAge	Reference=Hippocampus	−0.144	0.092	−1.558	0.119	[−0.325, 0.037]
Time	Reference=Hippocampus	0.181	0.048	3.77	<0.001***	[0.087, 0.275]
Time:region	Amygdala	−0.188	0.068	−2.774	0.006**	[−0.321, −0.055]
	Anterior cingulate	−0.299	0.068	−4.415	<0.001***	[−0.432, −0.166]
	Anterior compositus	−0.281	0.068	−4.142	<0.001***	[−0.414, −0.148]
	Caudate nucleus	−0.132	0.068	−1.954	0.051	[−0.265, 0.00]
	Ectosylvian	−0.226	0.068	−3.333	0.001***	[−0.359, −0.093]
	Entolateral	−0.163	0.068	−2.404	0.016*	[−0.296, −0.03]
	Genualis	−0.189	0.068	−2.782	0.005**	[−0.321, −0.056]
	Lateral fissure	−0.248	0.068	−3.666	<0.001***	[−0.381, −0.116]
	Medial cingulate	−0.27	0.068	−3.987	<0.001***	[−0.403, −0.137]
	Medial occipital	−0.231	0.068	−3.41	0.001**	[−0.364, −0.098]
	Orbital	−0.355	0.068	−5.236	<0.001***	[−0.488, −0.222]
	PR coronal	−0.196	0.068	−2.891	0.004**	[−0.329, −0.063]
	PR marginal	−0.254	0.068	−3.75	<0.001***	[−0.387, −0.121]
	Pararecurrens	−0.32	0.068	−4.715	<0.001***	[−0.452, −0.187]
	Posterior cingulate	−0.295	0.068	−4.353	<0.001***	[−0.428, −0.162]
	Posterior compositus	−0.373	0.068	−5.508	<0.001***	[−0.506, −0.24]
	Precruciate	−0.323	0.068	−4.772	<0.001***	[−0.456, −0.191]
	Pregenual	−0.37	0.068	−5.46	<0.001***	[−0.503, −0.237]
	Presplenial	−0.269	0.068	−3.972	<0.001***	[−0.402, −0.136]
	Proreus	−0.384	0.068	−5.666	<0.001***	[−0.517, −0.251]
	Recurrens	−0.327	0.068	−4.826	<0.001***	[−0.46, −0.194]
	Suprasylvian	−0.178	0.068	−2.633	0.008**	[−0.311, −0.046]
	Sylvian	−0.307	0.068	−4.527	<0.001***	[−0.44, −0.174]

Time-by-region interactions (time:region) thus represent the difference in volume change over time for a given region compared to the hippocampus. * $p < 0.05$, ** $p < 0.01$, *** $p < 0.001$.

Characterizing whole-brain spatiotemporal patterns of volume changes using DBM

Atlas-based approaches to assessing volumetry have their clear merits but run the risk of missing patterns or effects that do not correlate well with region boundaries, which motivated the use of whole-brain DBM. Thus, we conducted a voxel-wise LME analysis of the log-Jacobians or "DBM maps" that were generated from spatial registrations of the time point images to the SST and group template. We used a strict voxel-wise threshold of $p = 0.0001$ to identify clusters of the most extreme volume changes predicted by time, baseline age, and treatment by time interactions.

Consistent with the ROI-based LME analyses, post hoc linear contrasts examining differences from placebo for time-by-treatment interactions (tacrolimus-placebo minimum cluster size threshold = 29 mm³; Q134R-placebo minimum cluster size threshold = 15 mm³) did not yield any significant clusters of treatment-related effects on volume change by tacrolimus or by Q134R (data not shown).

Next, we wanted to examine cross-sectional aging effects on regional volume in the brain independent of longitudinal treatment effects. A cluster analysis of the log-Jacobians revealed five clusters for the main effect of age on volume decline
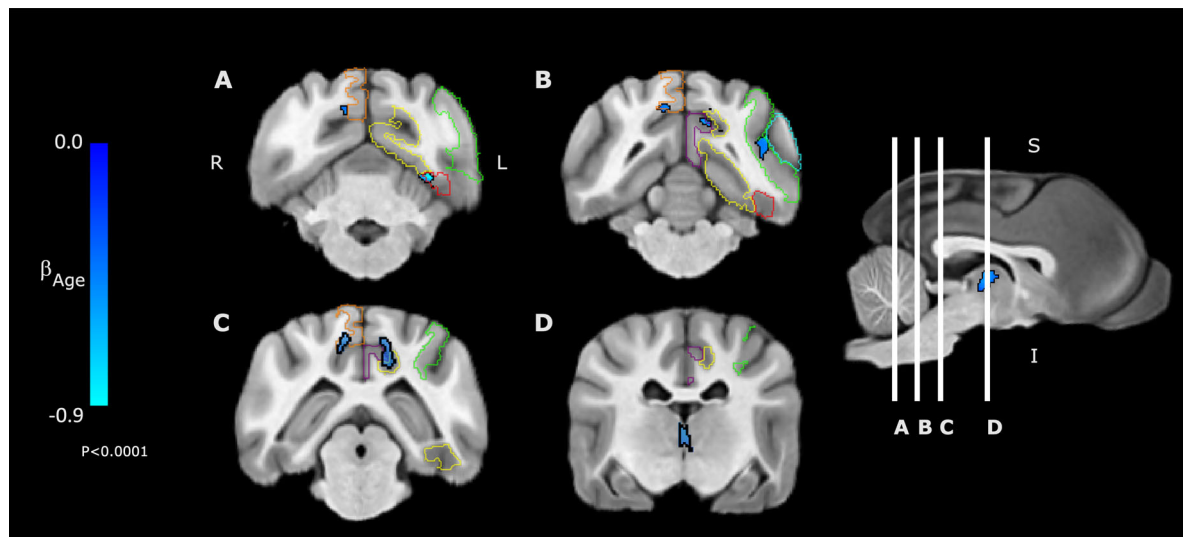
Figure 6. Linear mixed effects model parameter estimates for the main effect of age at baseline on log-Jacobian estimates for voxel-based volumes. Cross-sectional aging effects on volume decline were observed in various regions at baseline. Clusters shown with a black border indicate cross-sectional aging effects on reduced baseline volumes (log-Jacobian < 0; p < 0.0001) within (**A**) the left pararecurrens (red) and inferior medial occipital gyrus (yellow), (**B**) left occipital suprasylvian gyrus (green) and left ectosylvian gyrus (teal), (**C**) left medial occipital gyrus (yellow), left posterior cingulate gyrus (purple), and right occipital marginal gyrus (orange). Moreover, a cluster of volume loss was found over (**D**) the interthalamic adhesion (Dewey et al., 2020) which did not have a defined parcellation in the Johnson atlas. R, right; L, left; S, superior; I, inferior.

(log-Jacobian < 0) on all treatment groups with time fixed at baseline (minimum cluster-size threshold = 25 mm³). We found evidence of focal volume loss with every unit increase in age that was mainly posteriorly localized in the brain (Fig. 6A–D). The largest cluster of reduced volumes was found in the occipital marginal gyrus, medial occipital gyrus, and posterior cingulate gyrus in the left hemisphere (53 mm³; Fig. 6C), and the next largest cluster encompassed only the occipital marginal gyrus and the medial occipital gyrus in the right hemisphere (47 mm³; Fig. 6C). A smaller cluster spanning the occipital and temporal lobes was found within the left suprasylvian and ectosylvian gyri (35 mm³; Fig. 6B), and similar-sized cluster was found within the interthalamic adhesion (19 mm³; Fig. 6D). Lastly, a cluster within the left occipital lobe spanning the left inferior medial occipital gyrus and pararecurrens (16 mm³) had the most extreme age-related volume loss at baseline (Fig. 6A).

Next, to assess the volumetric changes over 3 years in the study which included behavioral enrichment across all groups, we performed a cluster analysis for the main effect of time from the DBM maps (minimum cluster-size threshold = 10 mm³; Fig. 7). Our DBM findings corroborated our ROI-based results where cortical shrinkage (log-Jacobian < 0) was the most prominent in frontal and temporal lobes. Furthermore, the greater spatial precision of this voxel-based volumetric estimation identified hotspots of volume loss within the posterior cingulate gyrus and the suprasylvian gyrus. The segmentation-agnostic DBM maps also allowed us to assess areas not defined by the Johnson atlas or ROIs that were previously excluded due to segmentation issues. We found rapid annual volume loss within the gyrus subproreus of the frontal lobe, the precruciate, pre- and postcentral gyri of the sensory-motor lobe, as well as significant volume loss within the genu, body, and splenium of the corpus callosum and within midbrain and brainstem areas. Cerebellum clusters are not shown.

Conversely, areas of significant expansion (log-Jacobian > 0) were observed over the lateral ventricles indicating ventricular widening, consistent with typical canine aging (Su et al., 2005; Gunde et al., 2020; Fig. 7). The hippocampus had significant

expansion along most of the dorsal hippocampus, but the ventral hippocampus was largely unchanged (Fig. 8). Furthermore, we found that the third ventricle immediately adjacent to dorsal hippocampus showed extreme volume loss which is consistent with dorsal hippocampal volume expansion. Lastly, we observed unexpected expansion across occipital and frontal white matter areas consistent with experience-dependent white matter plasticity (Mendez Colmenares et al., 2021; Fig. 7).

Discussion

In this study, we investigated cortical and subcortical volume changes in aging beagles, a natural model of AD (Cotman and Head, 2008; Vite and Head, 2014), undergoing long-term behavioral enrichment and tacrolimus, Q134R, or placebo treatment beginning in middle age. Our main goal was to explore the spatiotemporal patterns of brain atrophy in normal canine aging and assess the potential neuroprotective effects of CN/NFAT inhibitor treatment on brain volume. Using segmentation-based ROI volumetry and whole-brain, voxel-based DBM, we uncovered striking and unexpected evidence of increased bilateral hippocampal volume in all three groups across 3 years.

Our ROI-based evaluations showed that total hippocampal volume increased at an average rate of ~1.74% per year across treatment groups, contrasting with the age-related hippocampal volume decline observed in previous cross-sectional neuroimaging studies in laboratory beagles (Tapp et al., 2004). We did not observe any relationships between age and hippocampal volume at baseline prior to the behavioral enrichment protocol (Fig. 9), suggesting that the hippocampal volume increases were likely not a feature of typical hippocampal maturation in beagles. Instead, we argue that these increases may be attributed to the high levels of behavioral enrichment in the present study that included social interaction, exploration, physical exercise, and sensory stimulation, all of which are known to induce a number of neurobiological changes. Previous studies showed behaviorally enhanced adult neurogenesis in canines within the hilus of the dentate gyrus (DG) following behavioral enrichment (Siwak-
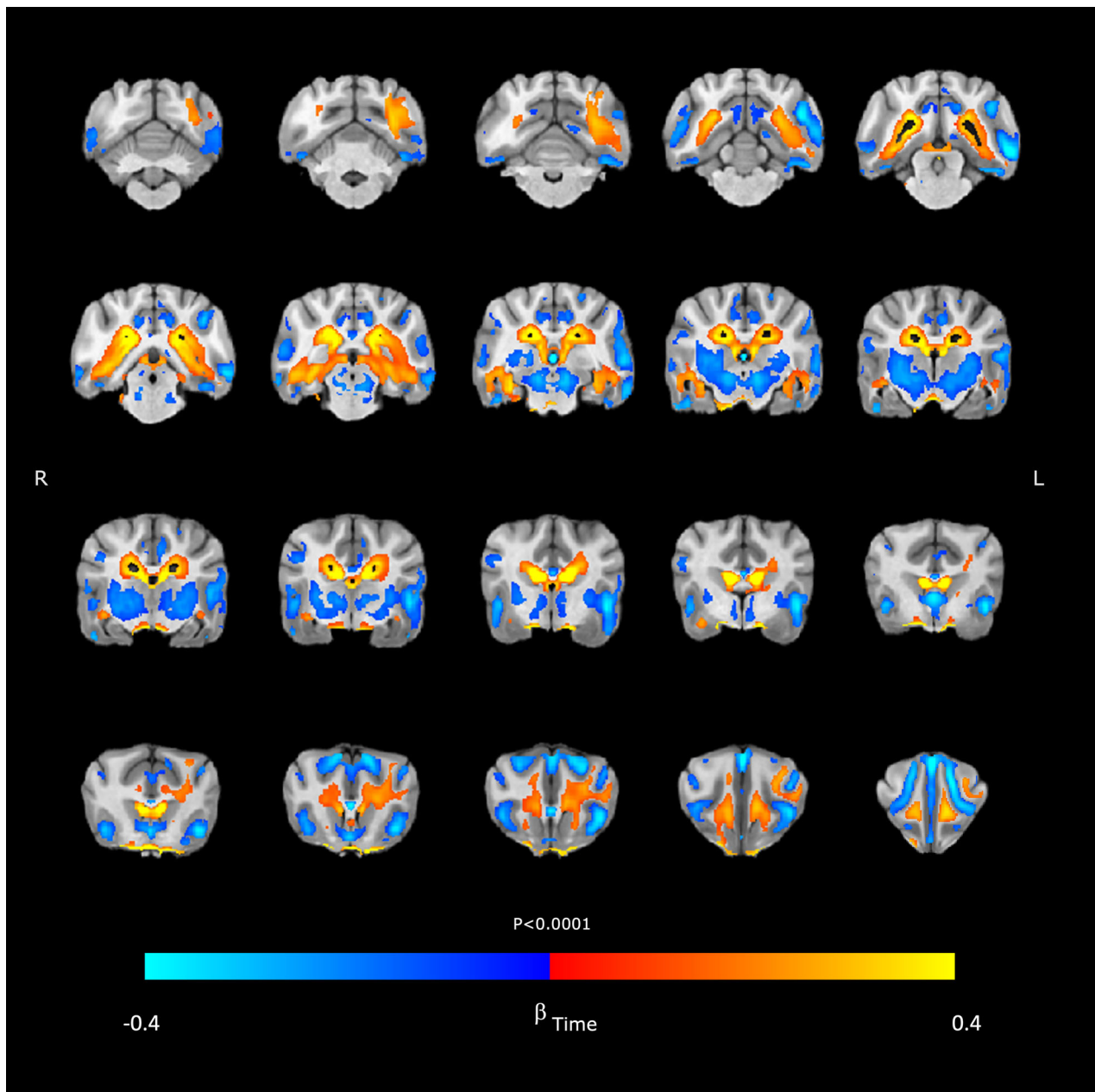
Figure 7. Linear mixed effects model parameter estimates for the main effect of time on log-Jacobian estimates for voxel-based volumes. Top row to bottom row, Posterior to anterior coronal views. Warm colors indicate volume increases over time (log-Jacobian > 0) and cool colors indicate volume losses over time (log-Jacobian < 0). We found areas of volume loss ($p < 0.0001$) across numerous cortical areas consistent with our ROI-based analysis and within regions not defined by the Johnson atlas including midbrain and corpus callosum. We also observed lateral ventricular widening and concurrent shrinkage of the third ventricle adjacent to dorsal hippocampus. Areas of select white matter expansion were observed within frontal and occipital lobes. R, right; L, left.

Tapp et al., 2008) and a dorsal-ventral gradient in neurogenic potential in the canine hippocampus (Bekiari et al., 2020). Although in the present study our DBM results showed volumetric increases that were mainly localized to dorsal hippocampus, whether these changes were primarily attributed to hippocampal neurogenesis is limited to speculation given the lack of a nonenriched control group in this study. Furthermore, other exercise-related angiogenic mechanisms such as vascular plasticity and increased cerebral blood volume may drive up hippocampal volume as well (Kim et al., 2021), which has been observed with high-resolution MRI in human adult exercise intervention studies (Maass et al., 2015). Whether angiogenesis and neurogenesis are interdependent mechanisms at play in the hippocampus,

or in other regions that possibly undergo adult neurogenesis such as the hypothalamus (Fowler et al., 2008), remains to be explored. A key aim of our histological analyses at the conclusion of the study will be to examine altered molecular and cellular signatures of neurogenesis related to CN/NFAT treatment which will be valuable to the growing body of research targeting neurogenic mechanisms in AD (Babcock et al., 2021).

We did not identify treatment-related modulation to hippocampal volume or to any other brain region by CN inhibition with tacrolimus or by NFAT inhibition with Q134R. However, our group has previously shown that multishell DWI, an imaging technique sensitive to microstructural gray and white matter changes (Alexander et al., 2007; Afzali et al., 2021;
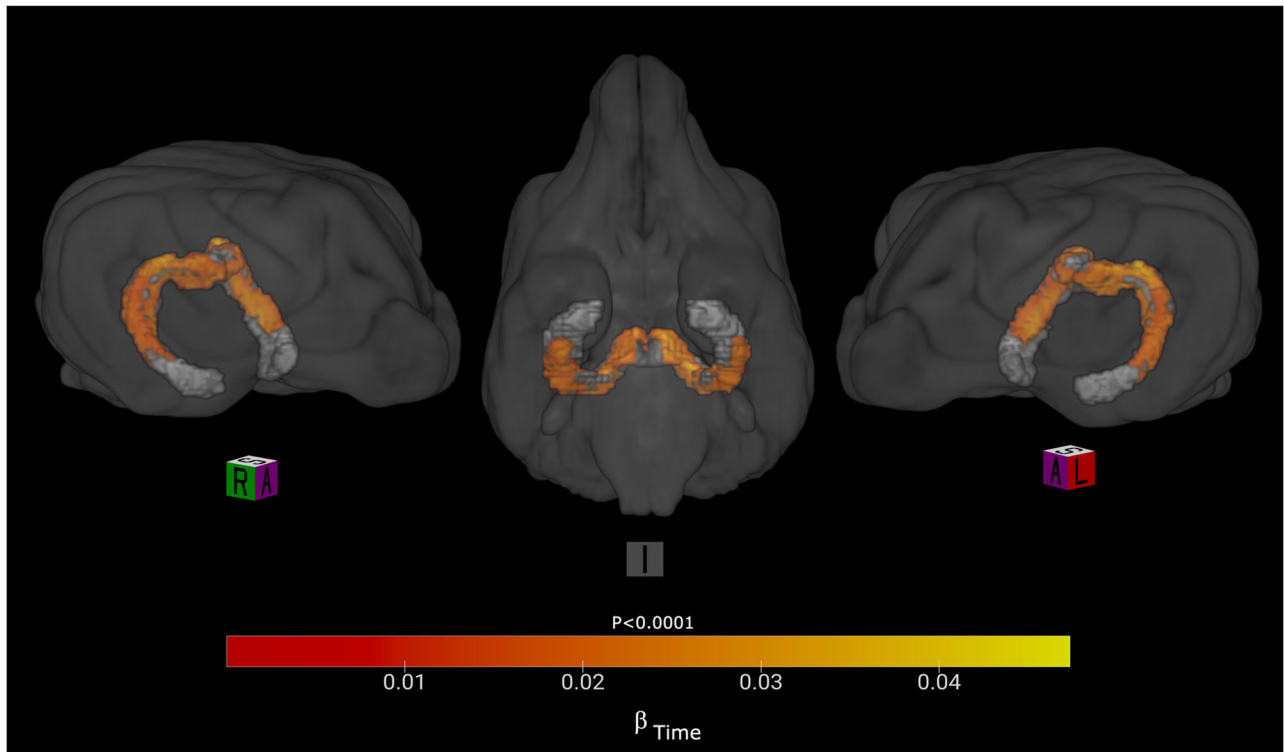
Figure 8. Volumetric increases mainly localized to dorsal hippocampus. Focusing on voxels representing significant volume change from the hippocampus, DBM revealed differential dorsal–ventral volume change with the greatest volume increases in dorsal hippocampus and volumetric preservation in the ventral hippocampus. Warmer colors indicate stronger volumetric increases. R, right; L, left; A, anterior; S, superior; I, inferior.

Radhakrishnan et al., 2022), showed age-related microstructural changes within the hippocampus, parahippocampal gyrus, and prefrontal cortex in placebo-treated dogs that were slower in tacrolimus-treated dogs after just 1 year (Radhakrishnan et al., 2021). Our negative finding with the current volumetric analysis is not surprising considering that tacrolimus, Q134R, and other peptide-based strategies targeting CN/NFAT-related signaling are known to affect cytoarchitectural and biochemical features including synaptic plasticity, neuroinflammation, and glutamate regulation (Dineley et al., 2007; Furman et al., 2012; Hudry et al., 2012; Sompol et al., 2017) that macrostructural measurements derived from T1-weighted imaging cannot detect. Furthermore, the majority of the dogs in this study had not yet reached the typical age where the effects of increasing Aβ burden such as oxidative stress, neurotoxicity, and neuronal loss become more prevalent, which begins ~9 years old for beagles (developmentally similar to 60-year-old humans; Cotman and Head, 2008). Thus, the final two MRI sessions for the dogs collected at mean ages of 10.5 and 11.5 years will offer greater insights into whether chronic CN/NFAT inhibition ameliorates impairments related to Aβ burden and/or ultimately slows the trajectory of age-related cortical and subcortical atrophy. Importantly, the lack of treatment effects on brain structure and age-associated volumetric losses suggests that although there may be no benefits currently on this outcome measure, long-term treatment with tacrolimus or Q134R does not appear to accelerate brain atrophy, which was recently found to be prevalent across numerous clinical trials for anti-Aβ therapies (Alves et al., 2023). However, we will continue to comprehensively monitor the safety and tolerability of these compounds following chronic administration in the aging beagles from neuroimaging and other standard safety measures.

Across all treatment groups, we observed volume losses across numerous cortical areas as well as ventricular enlargement, all consistent with prior reports of canine neuroimaging findings (Su et al., 1998; Kimotsuki et al., 2005). Importantly, our observations recapitulate the differential patterns of volume decline previously observed in aging beagles such as accelerated atrophy of the frontal lobe (Tapp et al., 2006). The prefrontal cortex is an early site of Aβ accumulation in both aging humans and canines (Head et al., 2000), which makes structural changes to this region an informative neuroimaging biomarker of potential AD-related neurodegeneration. Conversely, its preservation can be used as a biomarker of interest to distinguish effects of CNI or NFAT inhibitor treatment at the conclusion of the study. Interestingly, while a prior cross-sectional study by Tapp et al. (2004) suggests frontal lobe atrophy occurs ~10 years of age, their work did not include dogs between 7 and 9 years. Our longitudinal findings address this gap and suggest that the onset of frontal lobe volume decline occurs early during middle age, beginning as early as 5 years old in some of the dogs in the present study. Future work in comparison with nonenriched animals can shed light on whether the rate of frontal lobe volume loss may have been attenuated by enrichment.

The greater spatial sensitivity of the voxel-based DBM analysis revealed focal areas of significant age-related volume decline at baseline within the cingulate, occipital, and temporal lobes. Among these regions included the posterior cingulate gyrus, a region associated with early Aβ accumulation (Palmqvist et al., 2017), hypometabolism (Minoshima et al., 1997), synapse loss (Scheff and Price, 2001; Scheff et al., 2015), disrupted functional connectivity (Berron et al., 2020), and atrophy in the earliest phases of AD (Pengas et al., 2010). Prior work in beagles at
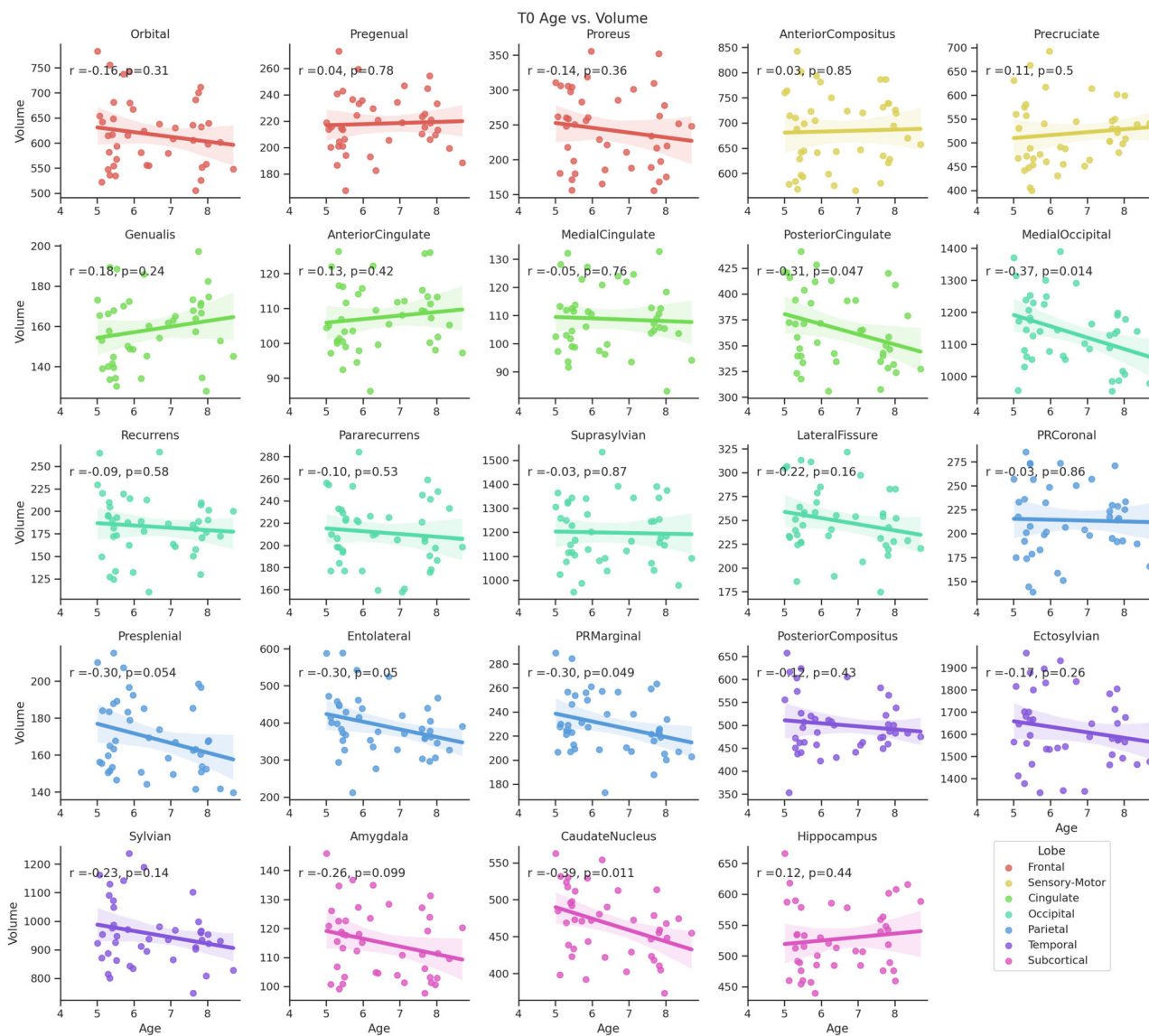
Figure 9. Baseline volumes by age. Scatterplots for age-by-volume correlations at baseline with Pearson's correlation coefficients (*r*) and *p* values (uncorrected). No correlations survive multiple comparisons with a Bonferroni's correction (*p* threshold = 0.002).

14 years old report extensive Aβ plaque aggregates in the cingulate cortex (Pop et al., 2012), but the time course of neurodegeneration in this region that may precede Aβ accumulation has not been characterized in beagles during middle age. Our findings provide the first in vivo evidence to our knowledge of posterior cingulate atrophy occurring as early as middle age that parallels human posterior cingulate atrophy and precedes frontal lobe atrophy in canines.

Furthermore, we identified novel volume preservation of the caudate nucleus. Interestingly, our baseline evaluation of cross-sectional volumes with respect to age showed a trend in caudate nucleus volume decline (Fig. 9), suggesting that exposure to our behavioral enrichment protocol may have contributed to its attenuation in volume changes across all groups (Fig. 5A,B). The caudate nucleus is part of an extensive prefrontal-striatal network that is involved in numerous functions, including coordination and motor planning (Fuster, 2002), and its volume steadily declines throughout human adulthood (Raz et al., 2003). In beagles, the caudate nucleus exhibits reduced glucose metabolism

by middle age (London et al., 1983) and along with the frontal cortex, is at risk for developing lesions in the form of lacunar infarcts or cysts (Su et al., 2005). More work is necessary to understand whether the preserved volumes of the caudate nucleus may be a result of daily exercise and training on numerous reward-based visuomotor tasks, similar to preservations previously observed in older human adults under long-term motor coordination training (Niemann et al., 2014).

Additionally, our voxel-wise DBM analysis also uncovered unexpected areas of white matter expansion among areas with well-documented white matter degradation in middle-aged humans (Raz et al., 2010). Long-term behavioral interventions such as training on a new visuomotor skill (Scholz et al., 2009), aerobic exercise (Mendez Colmenares et al., 2021), and memory training (De Lange et al., 2018) can induce white matter enhancements in human adults. DWI assessments are currently being performed in the dogs to further characterize these potential enrichment-associated alterations in both gray and white matter microstructure in greater detail.

Our ROI-based analyses were important descriptive analyses that can enhance statistical power by limiting the number of tests but can be prone to providing an incomplete picture by potentially artificially segregating the brain. Here, the problem was exacerbated by having several ROIs excluded on the basis of problematic segmentations during image preprocessing. A previous study comparing manual versus automated methods for brain extraction found that manual masking was still superior (Milne et al., 2016), indicating that more work is necessary for refining these image preprocessing procedures for canine data. Recently developed tools have leveraged deep learning for improving the accuracy of brain extraction performance (Tustison et al., 2021; Yu, Han, et al., 2022) but have been trained on human images and have yet to be adapted for canines. However, our novel application of DBM in the canine offers a more agnostic view to volumetric changes with greater spatial precision and was a valuable complementary approach for assessing morphometric alterations in the present study.

We were unable to perform any meaningful evaluations of sex differences because our cohort of dogs was predominantly female due to the availability of retired female breeders for the study. However, previous observations of sex differences in canine brain structure (Tapp et al., 2006) as well as the increasing proportion of women at risk for developing AD dementia over the next four decades compared with that of men (Rajan et al., 2021) suggest the need for future investigations to directly assess potential sex differences on drug efficacy in the canine model.

Our findings offer novel insights into in vivo volume changes that occur during middle age, prior to the known onset of major Aβ pathology in aging canines. We demonstrate the feasibility of an automated structural analysis pipeline to assess longitudinal changes in the canine brain at a high level of detail using state-of-the-art neuroimaging analysis tools designed to detect subtle alterations in brain morphology. The application of this analytical framework revealed both well-documented and novel structural alterations to the aging beagle brain and underscore the parallels of cortical and subcortical longitudinal changes in volume between canines and humans during aging. Our future application of this analytical framework will be instrumental for examining the utility of our in vivo neuroimaging biomarkers in predicting disease burden and cognitive outcomes under CN/NFAT inhibition. These findings in a natural model of AD like the beagle offer important contributions to the growing body of research aimed at understanding the role of modifiable lifestyle factors such as exercise, diet, and cognitive enrichment for reducing the risk of AD (Lista et al., 2015) and suggest that middle age may be a promising therapeutic window of behavioral intervention.

References

Abdul HM, et al. (2009) Cognitive decline in Alzheimer's disease is associated with selective changes in calcineurin/NFAT signaling. J Neurosci 29:12957–12969.

Abdul HM, Baig I, Levine H, Guttmann RP, Norris CM (2011) Proteolysis of calcineurin is increased in human hippocampus during mild cognitive impairment and is stimulated by oligomeric Abeta in primary cell culture. Aging Cell 10:103–113.

Afzali M, Pieciak T, Newman S, Garyfallidis E, Özarslan E, Cheng H, Jones DK (2021) The sensitivity of diffusion MRI to microstructural properties and experimental factors. J Neurosci Methods 347:108951.

Alexander AL, Lee JE, Lazar M, Field AS (2007) Diffusion tensor imaging of the brain. Neurotherapeutics 4:316–329.

Alves F, Kalinowski P, Ayton S (2023) Accelerated brain volume loss caused by anti–β-amyloid drugs: a systematic review and meta-analysis. Neurology 100:e2114–e2124.

Araujo JA, Segarra S, Mendes J, Paradis A, Brooks M, Thevarkunnel S, Milgram NW (2022) Sphingolipids and DHA improve cognitive deficits in aged beagle dogs. Front Vet Sci 9:646451.

Ashburner J, Hutton C, Frackowiak R, Johnsrude I, Price C, Friston K (1998) Identifying global anatomical differences: deformation-based morphometry. Hum Brain Mapp 6:348–357.

Avants BB, Tustison NJ, Wu J, Cook PA, Gee JC (2011) An open source multivariate framework for n-tissue segmentation with evaluation on public data. Neuroinformatics 9:381–400.

Babcock KR, Page JS, Fallon JR, Webb AE (2021) Adult hippocampal neurogenesis in aging and Alzheimer's disease. Stem Cell Rep 16:681–693.

Bekiari C, Grivas I, Tsingotjidou A, Papadopoulos GC (2020) Adult neurogenesis and gliogenesis in the dorsal and ventral canine hippocampus. J Comp Neurol 528:1216–1230.

Berron D, van Westen D, Ossenkoppele R, Strandberg O, Hansson O (2020) Medial temporal lobe connectivity and its associations with cognition in early Alzheimer's disease. Brain 143:1233–1248.

Buckner RL, Head D, Parker J, Fotenos AF, Marcus D, Morris JC, Snyder AZ (2004) A unified approach for morphometric and functional data analysis in young, old, and demented adults using automated atlas-based head size normalization: reliability and validation against manual measurement of total intracranial volume. NeuroImage 23:724–738.

Chan ADF, Nippak PMD, Murphey H, Ikeda-Douglas CJ, Muggenburg B, Head E, Cotman CW, Milgram NW (2002) Visuospatial impairments in aged canines (Canis familiaris): the role of cognitive-behavioral flexibility. Behav Neurosci 116:443–454.

Chen G, Saad ZS, Britton JC, Pine DS, Cox RW (2013) Linear mixed-effects modeling approach to FMRI group analysis. NeuroImage 73:176–190.

Christie LA, Saunders RC, Kowalska DM, MacKay WA, Head E, Cotman CW (2008) Rhinal and dorsolateral prefrontal cortex lesions produce selective impairments in object and spatial learning and memory in canines. J Comp Neurol 511:257–270.

Congdon EE, Sigurdsson EM (2018) Tau-targeting therapies for Alzheimer disease. Nat Rev Neurol 14:399–415.

Cotman CW, Head E (2008) The canine (Dog) model of human aging and disease: dietary, environmental and immunotherapy approaches. J Alzheimer's Dis 15:685–707.

Crous-Bou M, Minguillón C, Gramunt N, Molinuevo JL (2017) Alzheimer's disease prevention: from risk factors to early intervention. Alzheimer's Res Ther 9:71.

Czeibert K, Andics A, Petneházy Ö, Kubinyi E (2019) A detailed canine brain label map for neuroimaging analysis. Biol Futura 70:112–120.

Datta R, Lee J, Duda J, Avants BB, Vite CH, Tseng B, Gee JC, Aguirre GD, Aguirre GK (2012) A digital atlas of the dog brain. PLoS ONE 7:e52140.

Davis PR, et al. (2017) Aβ vaccination in combination with behavioral enrichment in aged beagles: effects on cognition, Aβ, and microhemorrhages. Neurobiol Aging 49:86–99.

De Lange A-MG, Bråthen ACS, Rohani DA, Fjell AM, Walhovd KB (2018) The temporal dynamics of brain plasticity in aging. Cereb Cortex 28:1857–1865.

Dineley KT, Hogan D, Zhang W-R, Taglialatela G (2007) Acute inhibition of calcineurin restores associative learning and memory in Tg2576 APP transgenic mice. Neurobiol Learn Mem 88:217–224.

Fowler CD, Liu Y, Wang Z (2008) Estrogen and adult neurogenesis in the amygdala and hypothalamus. Brain Res Rev 57:342–351.

Furman JL, Sama DM, Gant JC, Beckett TL, Murphy MP, Bachstetter AD, Van Eldik LJ, Norris CM (2012) Targeting astrocytes ameliorates neurologic changes in a mouse model of Alzheimer's disease. J Neurosci 32:16129–16140.

Fuster JM (2002) Frontal lobe and cognitive development. J Neurocytol 31:373–385.

González-Soriano J, Marín García P, Contreras-Rodríguez J, Martínez-Sainz P, Rodríguez-Veiga E (2001) Age-related changes in the ventricular system of the dog brain. Ann Anat 183:283–291.

Gross B, Garcia-Tapia D, Riedesel E, Ellinwood NM, Jens JK (2010) Normal canine brain maturation at magnetic resonance imaging: MRI appearance of normal postnatal canine brain maturation with histology correlation. Vet Radiol Ultrasound 51:361–373.

Gunde E, Czeibert K, Gábor A, Szabó D, Kis A, Arany-Tóth A, Andics A, Gácsi M, Kubinyi E (2020) Longitudinal volumetric assessment of ventricular enlargement in pet dogs trained for functional magnetic resonance imaging (fMRI) studies. Vet Sci 7:127.

Hackler L, Gyuris M, Huzián O, Alföldi R, Szebeni GJ, Madácsi R, Knapp L, Kanizsai I, Puskás LG (2019) Enantioselective synthesis of 8-hydroxyquinoline derivative, Q134 as a hypoxic adaptation inducing agent. Molecules 24:23.

Head E, et al. (2008) A Two-year study with fibrillar β-amyloid (Aβ) immunization in aged canines: effects on cognitive function and brain Aβ. J Neurosci 28:3555–3566.

Head E, Callahan H, Muggenburg BA, Cotman CW, Milgram NW (1998) Visual-discrimination learning ability and β-amyloid accumulation in the dog. Neurobiol Aging 19:415–425.

Head E, McCleary R, Hahn FF, Milgram NW, Cotman CW (2000) Region-specific age at onset of β-amyloid in dogs★. Neurobiol Aging 21:89–96.

Hudry E, Wu H-Y, Arbel-Ornath M, Hashimoto T, Matsouaka R, Fan Z, Spires-Jones TL, Betensky RA, Bacskai BJ, Hyman BT (2012) Inhibition of the NFAT pathway alleviates amyloid β neurotoxicity in a mouse model of Alzheimer's disease. J Neurosci 32:3176–3192.

Johnson PJ, Luh W-M, Rivard BC, Graham KL, White A, FitzMaurice M, Loftus JP, Barry EF (2020) Stereotactic cortical atlas of the domestic canine brain. Sci Rep 10:4781.

Kim TA, Chen L, Ge S (2021) The interplay of neurovasculature and adult hippocampal neurogenesis. Neurosci Lett 760:136071.

Kimotsuki T, Nagaoka T, Yasuda M, Tamahara S, Matsuki N, Ono K (2005) Changes of magnetic resonance imaging on the brain in beagle dogs with aging. J Vet Med Sci 67:961–967.

Kuchibhotla KV, Goldman ST, Lattarulo CR, Wu H-Y, Hyman BT, Bacskai BJ (2008) Abeta plaques lead to aberrant regulation of calcium homeostasis in vivo resulting in structural and functional disruption of neuronal networks. Neuron 59:214–225.

Lista S, Dubois B, Hampel H (2015) Paths to Alzheimer's disease prevention: from modifiable risk factors to biomarker enrichment strategies. J Nutr Health Aging 19:154–163.

London ED, Ohata M, Takei H, French AW, Rapoport SI (1983) Regional cerebral metabolic rate for glucose in beagle dogs of different ages. Neurobiol Aging 4:121–126.

Maass A, et al. (2015) Vascular hippocampal plasticity after aerobic exercise in older adults. Mol Psychiatry 20:585–593.

Martinez MN, Mochel JP, Neuhoff S, Pade D (2021) Comparison of canine and human physiological factors: understanding interspecies differences that impact drug pharmacokinetics. AAPS J 23:59.

Mendez Colmenares A, Voss MW, Fanning J, Salerno EA, Gothe NP, Thomas ML, McAuley E, Kramer AF, Burzynska AZ (2021) White matter plasticity in healthy older adults: the effects of aerobic exercise. NeuroImage 239:118305.

Milgram NW, Adams B, Callahan H, Head E, Mackay B, Thirlwell C, Cotman CW (1999) Landmark discrimination learning in the dog. Learn Mem 6:54–61.

Milne ME, Steward C, Firestone SM, Long SN, O'Brien TJ, Moffat BA (2016) Development of representative magnetic resonance imaging–based atlases of the canine brain and evaluation of three methods for atlas-based segmentation. Am J Vet Res 77:395–403.

Minoshima S, Giordani B, Berent S, Frey KA, Foster NL, Kuhl DE (1997) Metabolic reduction in the posterior cingulate cortex in very early Alzheimer's disease. Ann Neurol 42:85–94.

Niemann C, Godde B, Staudinger UM, Voelcker-Rehage C (2014) Exercise-induced changes in basal ganglia volume and cognition in older adults. Neuroscience 281:147–163.

Norris CM, Kadish I, Blalock EM, Chen K-C, Thibault V, Porter NM, Landfield PW, Kraner SD (2005) Calcineurin triggers reactive/inflammatory processes in astrocytes and is upregulated in aging and Alzheimer's models. J Neurosci 25:4649–4658.

O'Brien RM (2017) Mixed models, linear dependency, and identification in age-period-cohort models: mixed models and identification in age-period-cohort models. Stat Method 36:2590–2600.

Palmqvist S, Schöll M, Strandberg O, Mattsson N, Stomrud E, Zetterberg H, Blennow K, Landau S, Jagust W, Hansson O (2017) Earliest accumulation of β-amyloid occurs within the default-mode network and concurrently affects brain connectivity. Nat Commun 8:1.

Pengas G, Hodges JR, Watson P, Nestor PJ (2010) Focal posterior cingulate atrophy in incipient Alzheimer's disease. Neurobiol Aging 31:25–33.

Perl DP (2010) Neuropathology of Alzheimer's disease. Mt Sinai J Med 77:32–42.

Pop V, Head E, Berchtold NC, Glabe CG, Studzinski CM, Weidner AM, Murphy MP, Cotman CW (2012) Aβ aggregation profiles and shifts in APP processing favor amyloidogenesis in canines. Neurobiol Aging 33:108–120.

Radhakrishnan H, et al. (2021) Tacrolimus protects against age-associated microstructural changes in the beagle brain. J Neurosci 41:5124–5133.

Radhakrishnan H, Bennett IJ, Stark CE (2022) Higher-order multi-shell diffusion measures complement tensor metrics and volume in gray matter when predicting age and cognition. NeuroImage 253:119063.

Rajan KB, Weuve J, Barnes LL, McAninch EA, Wilson RS, Evans DA (2021) Population estimate of people with clinical AD and mild cognitive impairment in the United States (2020–2060). Alzheimer Dement 17:1966–1975.

Randhawa PS, Starzl TE, Demetris AJ (1997) Tacrolimus (FK506)-associated renal pathology. Adv Anat Pathol 4:265–276.

Raz N, Ghisletta P, Rodrigue KM, Kennedy KM, Lindenberger U (2010) Trajectories of brain aging in middle-aged and older adults: regional and individual differences. NeuroImage 51:501–511.

Raz N, Rodrigue KM, Kennedy KM, Head D, Gunning-Dixon F, Acker JD (2003) Differential aging of the human striatum: longitudinal evidence. Am J Neuroradiol 24:1849–1856.

Reese LC, Taglialatela G (2010) Neuroimmunomodulation by calcineurin in aging and Alzheimer's disease. Aging Dis 1:245–253.

Rofina JE, van Ederen AM, Toussaint MJM, Secrève M, van der Spek A, van der Meer I, Van Eerdenburg FJCM, Gruys E (2006) Cognitive disturbances in old dogs suffering from the canine counterpart of Alzheimer's disease. Brain Res 1069:216–226.

Scheff SW, Price DA (2001) Alzheimer's disease-related synapse loss in the cingulate cortex. J Alzheimer's Dis 3:495–505.

Scheff SW, Price DA, Ansari MA, Roberts KN, Schmitt FA, Ikonomovic MD, Mufson EJ (2015) Synaptic change in the posterior cingulate gyrus in the progression of Alzheimer's disease. J Alzheimer's Dis 43:1073–1090.

Scholz J, Klein MC, Behrens TE, Johansen-Berg H (2009) Training induces changes in white-matter architecture. Nat Neurosci 12:1370–1371.

Siwak-Tapp CT, Head E, Muggenburg BA, Milgram NW, Cotman CW (2008) Region specific neuron loss in the aged canine hippocampus is reduced by enrichment. Neurobiol Aging 29:39–50.

Sompol P, et al. (2017) Calcineurin/NFAT signaling in activated astrocytes drives network hyperexcitability in Aβ-bearing mice. J Neurosci 37:6132–6148.

Sompol P, et al. (2021) Q134r: small chemical compound with NFAT inhibitory properties improves behavioral performance and synapse function in mouse models of amyloid pathology. Aging Cell 20:e13416.

Song Z, Krishnan A, Gaetano L, Tustison NJ, Clayton D, de Crespigny A, Bengtsson T, Jia X, Carano RAD (2022) Deformation-based morphometry identifies deep brain structures protected by ocrelizumab. NeuroImage Clin 34:102959.

Stallings NR, O'Neal MA, Hu J, Shen Z-J, Malter JS (2023) Long-term normalization of calcineurin activity in model mice rescues Pin1 and attenuates Alzheimer's phenotypes without blocking peripheral T cell IL-2 response. Alzheimer's Res Ther 15:179.

Studzinski C, Christie L, Araujo J, Burnham W, Head E, Cotman C, Milgram N (2006) Visuospatial function in the beagle dog: an early marker of cognitive decline in a model of human aging and dementia. Neurobiol Learn Mem 86:197–204.

Su M-Y, et al. (2005) A longitudinal study of brain morphometrics using serial magnetic resonance imaging analysis in a canine model of aging. Prog Neuro-Psychopharmacol Biol Psychiatry 29:389–397.

Su M-Y, Head E, Brooks WM, Wang Z, Muggenburg BA, Adam GE, Sutherland R, Cotman CW, Nalcioglu O (1998) Magnetic resonance imaging of anatomic and vascular characteristics in a canine model of human aging. Neurobiol Aging 19:479–485.

Taglialatela G, Hogan D, Zhang W-R, Dineley KT (2009) Intermediate- and long-term recognition memory deficits in Tg2576 mice are reversed with acute calcineurin inhibition. Behav Brain Res 200:95–99.

Taglialatela G, Rastellini C, Cicalese L (2015) Reduced incidence of dementia in solid organ transplant patients treated with calcineurin inhibitors. J Alzheimer's Dis 47:329–333.

Tapp PD, Head K, Head E, Milgram NW, Muggenburg BA, Su M-Y (2006) Application of an automated voxel-based morphometry technique to assess regional gray and white matter brain atrophy in a canine model of aging. NeuroImage 29:234–244.

Tapp PD, Siwak CT, Estrada J, Head E, Muggenburg BA, Cotman CW, Milgram NW (2003) Size and reversal learning in the beagle dog as a

measure of executive function and inhibitory control in aging. Learn Mem 10:64–73.

Tapp PD, Siwak CT, Gao FQ, Chiou J-Y, Black SE, Head E, Muggenburg BA, Cotman CW, Milgram NW, Su M-Y (2004) Frontal lobe volume, function, and β-amyloid pathology in a canine model of aging. J Neurosci 24:8205–8213.

Tustison NJ, et al. (2014) Large-scale evaluation of ANTs and FreeSurfer cortical thickness measurements. Neuroimage 99:166–179.

Tustison NJ, et al. (2021) The ANTsX ecosystem for quantitative biological and medical imaging. Sci Rep 11:9068.

Tustison NJ, Avants BB, Cook PA, Zheng Y, Egan A, Yushkevich PA, Gee JC (2010) N4ITK: improved N3 bias correction. IEEE Trans Med Imaging 29:1310–1320.

Tustison NJ, Holbrook AJ, Avants BB, Roberts JM, Cook PA, Reagh ZM, Duda JT, Stone JR, Gillen DL, Yassa MA (2019) Longitudinal mapping of cortical thickness measurements: an Alzheimer's disease neuroimaging initiative-based evaluation study. J Alzheimer's Dis 71: 165–183.

Vite CH, Head E (2014) Aging in the canine and feline brain. Vet Clin North Am Small Anim Pract 44:1113–1129.

Yu Z, Guindani M, Grieco SF, Chen L, Holmes TC, Xu X (2022) Beyond t test and ANOVA: applications of mixed-effects models for more rigorous statistical analysis in neuroscience research. Neuron 110:21–35.

Yu Z, Han X, Xu W, Zhang J, Marr C, Shen D, Peng T, Zhang X-Y, Feng J (2022) A generalizable brain extraction net (BEN) for multimodal MRI data from rodents, nonhuman primates, and humans. eLife 11:e81217.